

Optical measurements of bubbles and spray in wind/water facilities at high wind speeds

W. Mischler*, B. Jähne

HCI & IUP, University of Heidelberg, Germany

wolfgang.mischler@iwr.uni-heidelberg.de and bernd.jaehne@iwr.uni-heidelberg.de

Abstract

An optical technique to measure the size distribution and velocity of bubbles and spray is presented and evaluated. A bright field setup with a matched telecentric lens and illumination is used. The hardware was optimized to get high quality data and to allow for velocity measurements of particles. Several image processing algorithms for determining radius, position and velocity of particles were developed and evaluated. The presented technique has an error in size below 1% for particles bigger than 10 px and an error below 10% for smaller particles with a smallest detectable radius of 3 px. First experimental results from the new Kyoto High Wind-Speed wind-wave facility (bubble measurements) and the Heidelberg linear wind-wave facility (spray measurements) show the high potential of the new technique.

Introduction

This setup is intended to be used in wind wave channels in the environmental sciences. In these channels wind induced spray and bubbles generated by breaking waves are characterized. This data can be used to get further insights into mechanisms of gas and heat transfer on the water surface between ocean and atmosphere. You can imagine this by thinking of the bubbles as an additional exchange surface, which participates only for finite amount of time in the transport processes.

Since breaking waves produce a wide spectrum of bubble sizes ranging from micrometers to centimeters [2], it is necessary to use a measurement technique, capable to resolve a wide radius range. At the same time it has to be able to handle non spherical objects and detect anomalies, like waves, which distort the optical path in a complex way.

In the past, bubbles have been measured in laboratory wind-wave facilities with fiber probes, acoustically, laser doppler anemometry (LDA) or phase doppler anemometry (PDA). Fiber probes are easy to deploy and robust, but are intrusive and have a small measurement volume [10]. Acoustical measurements are also intrusive and do not work well for non-spherical bubbles [11]. LDA is an established method for velocity field measurements, but lacks the ability to determine the radius of the particles. PDA eliminates this disadvantage, but works only for spherical objects [7]. Imaging techniques can overcome these difficulties as the large amount of sensors (i.e. pixels) allows for sophisticated evaluation strategies. In this work, a setup is presented which is capable of measuring a wide range of particle sizes, while not being intrusive.

Experimental Methods

The measurement setup, which is based on the earlier work of Jähne and Geißler 1994 [5], is shown in figure 1. A CMOS camera is looking through the measurement volume into a pulsed light source. A matched telecentric illumination and imaging system is used with parallel principal rays of small angular aperture. This guarantees constant magnification within the measurement volume at the working distance (135mm). The bubbles appear as black areas in the images (see figure 2), because the bubbles reflect resp. refract the parallel rays out of the optical path. Illuminations with a greater angular aperture would image the bubbles as dark contours.

A blue LED (Cree XP-E) is used as a light source and is placed in the focal plane of an optics with an aperture of 50mm, which defines the maximal measurement area. Since a pulsed high power LED is used, effective exposure times, i.e. the time the LED is switched on, of a few μ s are possible. To measure the size distributions in a sense of a density, it is also necessary to know the effective measurement volume. While the size of the image plane is determined by the magnification, the 3rd dimension z depends on the processing of the images. Since we assume the particles to be black discs, we take the blurring of the edge of the discs as a measure for the z component.

For the measurements a Basler acA2000-340km camera with 2048 px \times 1088 px, 5.5 μ m \times 5.5 μ m each, was used, where one pixel corresponds to 14.63 μ m in object space. To acquire velocity data two subsequent images, with a small known temporal distance (typical value: 2 ms) were taken. Finding corresponding particles in the image yields the velocity components of the particles in the image plane (see fig. 2 right). The principle how to get

*Corresponding author: wolfgang.mischler@iwr.uni-heidelberg.de

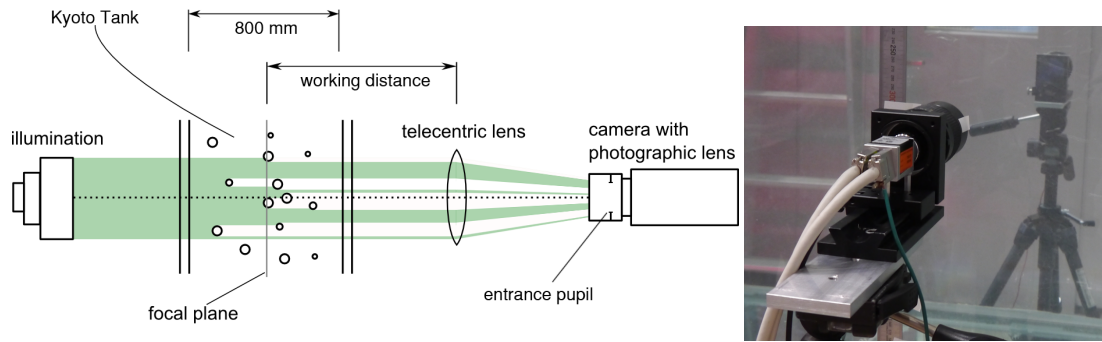


Figure 1. *left:* Illustration of the measurement setup. On one side of the measurement tank the illumination is placed. On the opposite side the camera with the optics is mounted. *right:* Photograph of the measurement setup, as used in the measurements in Kyoto. In front of the picture you can see the camera, in the rear you can see the illumination.

two images rapidly one after another is illustrated in fig. 3. The camera exposure is set to the maximum possible value that the given frame rate allows. From the triggered light source, one pulse is sent at the end of the first frame and the second is sent at the start of the second frame. With this timing, called image straddling, periods down to one μ s are possible here.

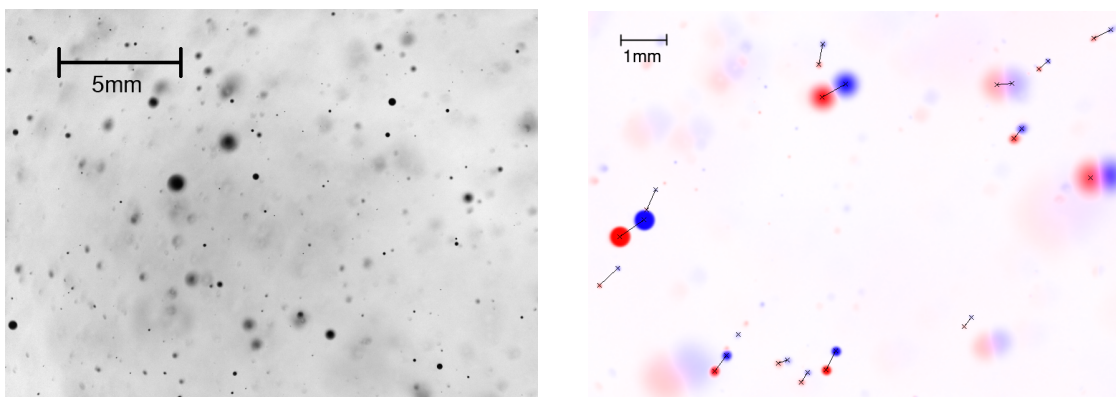


Figure 2. *left:* Sample images (normalized) of a bubble measurement. *right:* overlay of two subsequent images for velocity measurements. The blue image was recorded 5 ms earlier than the red one. The assignment of corresponding bubbles was done by finding the nearest neighbor.

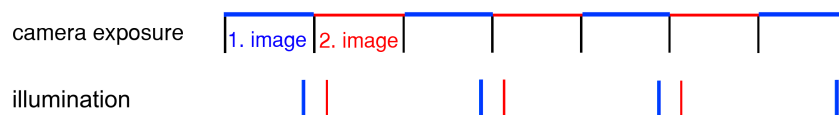


Figure 3. Timing of camera exposure and illumination for velocity measurements. It is shown that the shutter of the camera is almost always open, while the illumination generates two subsequent images in a short time interval.

Evaluation algorithms

In this section three approaches to evaluate the acquired images are presented. The goal is to determine the number, size and velocity **and** the measurement volume of the particles. All approaches share the pre and post processing. Pre processing improves image quality, removes noise and normalizes the images. For the actual particle detection three approaches were tested, which will be described below. The idea is the same for all three:

segment the image with a threshold and calculate individual features for all objects^{*}. That means the performance of the algorithms depends on the choice of these features. The post processing is used to extract the relevant data from the features and visualize it. The components of the several parts are described in the following:

Pre processing

In this processing step all images are normalized to values ideally ranging from 0.0 (background) to 1.0 (object). Therefore a 2-point calibration with a dark image g_Z and a zero image g_D , i.e. an image with illumination, but no particles is made. The normalized image $n(x, y)$ results from the raw image $g(x, y)$ by:

$$n(x, y) = 1 - \frac{g(x, y) - g_D(x, y)}{g_Z(x, y) - g_D(x, y)}. \quad (1)$$

To remove high frequency noise a binomial filter with width 8 is applied. Due to the long optical path through the measurement tank and/or high particle densities, it is common that the average gray value level of the background increases and the level of the objects decreases for the normalized images[†]. To compensate for that, a simple gray value scaling, here called drift correction, is applied, so that the histogram peak of the background has a value of 0.0 and the maximum value of the image is at 1.0.

Processing

With these images each of the following algorithms tries to evaluate the wanted parameters radius r , distance from focal plane z , segmented area A and a quality indicator. The necessity for A and the quality indicator will be explained in the post-processing step. Each of the algorithms starts with a segmentation with a global threshold or value range. At this point the different algorithms will be explained separately:

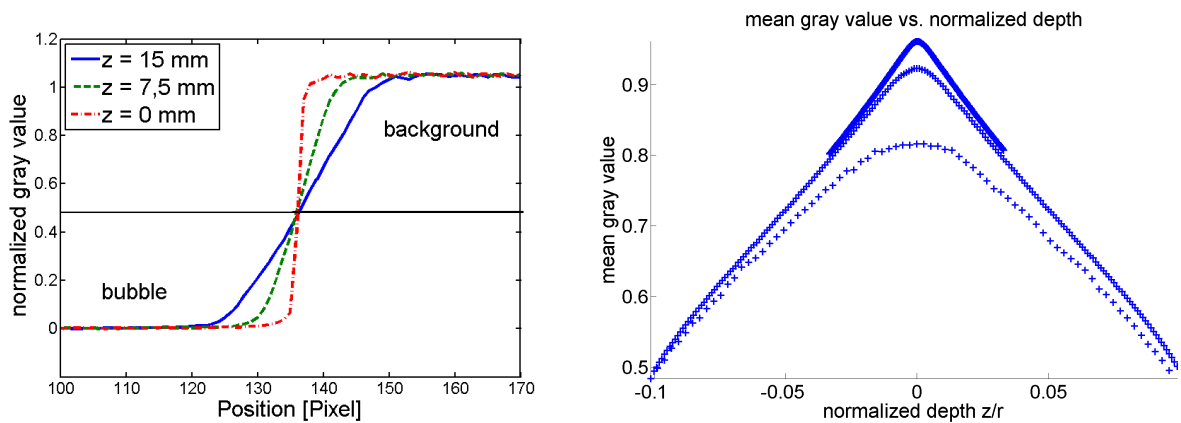


Figure 4. *left:* Illustration of the gray values produced by edges in different distances z to the optics. The gradient decreases with increasing distance from focal plane. There is a gray value for which the position of the edge does not move (intersection of the curves). *right:* dependency of the mean gray value on the normalized distance for different radii. It is linear (but ambiguous in the distance), and can thus be used to determine z . The reason for some of the data decreasing around zero distance, is that these data is from bubbles smaller than 150 μm . These do not fulfill the condition of reaching the maximum gray value in their center, so the model begins to fail. This effect is corrected according to 1.

Variant 1 segments the image with a global threshold. Since we are using a telecentric optic, we can determine the distance from the focal plane of the particles under certain circumstances. As can be seen in fig. 4 left, the gradient of the gray value on an imaged edge depends on the distance from the focal plane. Additionally at the position of the edge the normalized gray value is constant. The telecentric illumination guarantees that the bubble images have sharp edges and blurring only occurs when bubbles are out of focus. Therefore these effects can be utilized to determine the distance and the size of the particles. For a detailed derivation of these effect see [6] and [9]. The threshold in this algorithm is chosen to be the value of fixed position of the edge, so we get an unbiased area of the bubble. After applying a morphological closing to the segmented image to reduce noise, the objects are

^{*}Algorithm 2 includes additionally a method for separating overlapping particles

[†]for raw images the opposite is true, because of the first minus in eq. 1.

labeled. For each object, the total area in pixels is determined, which yields the radius with a given magnification factor. For determining the distance from the focal plane the mean gray value \bar{g} is determined. The further the particle is away from the focal plane, the more pixels have normalized gray values smaller than 1 (see fig. 4 left). Figure 4 right, shows that the mean gray value \bar{g} is linearly dependent on the normalized distance from the focal plane, $\frac{z}{r}$. For small bubbles the assumption that they reach maximum gray value in their center is no longer fulfilled. These particles follow curves that are lower than the linear behavior, which can also be seen in fig. 4 right. This effect is corrected according to 1. As an quality indicator the gray value at the center of the object g_C is stored, since it is shown in [8], that the assumptions made here hold, only if the center pixel reaches its maximum. For eventual velocity calculations the centers of gravity are also stored.

Variant 2 tries to overcome one limitation of Variant 1: At high particle densities, particles overlap frequently in the images. Variant 1 will then either reject those non-spherical particles (based on an eigenvalue analysis) or determine a wrong radius. Variant 2 determines the contour of the objects that are segmented as in Variant 1. Overlapping bubbles are separated using a method described in [4]. The implementation of the algorithm is described in detail in [8]. Here, only a brief summary is given: On the contour of overlapping bubbles, points of high curvature are detected. The contour segments to the left and right of these points likely belong to different bubbles. The contour is split and individual circles[‡] are fitted to each segment. These circles are clustered (since each bubble can have multiple segments) based on the center of the fitted circle. Position and radius r^* of each cluster are stored together with the area of the original object A and the gray value at the center of the fitted circle g_C . The distance from the focal plane can now be determined from the mean gradient on the contour of the bubbles, the stronger the gradient, the closer to the focal plane (see [8]).

Variant 3 is designed to be complementary to Variant 1 and 2. Since the other two algorithms fail for small bubbles, which do not reach the maximum in their center pixels, additionally this approach is used. Variant 3 uses a lower segmentation threshold, the boundary is set to be at least five times the standard deviation of the background noise. Objects that reach the maximum gray value (and thus are detected by Variant 1 and Variant 2) are discarded to avoid double counts. As in Variant 1 the features are calculated, supplemented with the value of a Laplace filtered image at the center of the object. Since the position of the edge is not constant in changing distances another combination of features is used as a measure for the radius. Here the sum of the gray values, which equals $A \cdot \bar{g}$, is used. This represents the total energy ascribed[§] to one particle with a given size. This should be preserved and thus can be used as a measure for the radius.

Post processing

Once the data for the single particles is gathered, the velocity and the size distribution of the particles can be calculated. Corresponding bubbles in subsequent images for the velocity measurement are chosen to be the nearest neighbor according to the L_2 -norm in (x,y,r) -space[¶].

To measure bubble densities, it is necessary to know the measurement volume. Thus we need to know in which volume the algorithms are able to detect bubbles. The maximum distance z_{\max} from the focal plane at which bubbles of radius r can be detected is determined by calibration (see fig. 7). In the direction parallel to the focal plane, the measurement area is smaller than the area that is visible in the image for two reasons:

a) Bubbles whose center is outside the image are rejected, thus for a bubble radius r the image size is reduced by a band of width r along the image boundary.

b) Small particles can be occluded by bigger particles. This can be corrected by sorting all detected particles descendant by size and introducing effective measurement areas $A_{\text{eff},i}$:

$$A_{\text{eff},i} = A - \sum_{i < j} A_j, \quad (2)$$

The measurement area for bubble i $A_{\text{eff},i}$ is the total area minus the sum of the segmented areas A_j that are covered with bigger bubbles. If all areas had the same size, the particle area density would be n/A , where n is the number of detected objects in the desired radius interval. With varying measurement areas, all effective measurement areas $A_{\text{eff},i}$ of objects within this radius interval are added inversely, to get the density Ψ :

$$\Psi = \frac{1}{A_{1,\text{eff}}} + \frac{1}{A_{2,\text{eff}}} + \dots + \frac{1}{A_{n,\text{eff}}} \approx \frac{n}{A}, \quad \text{for small bubbles} \quad (3)$$

[‡]it is also possible to fit ellipses

[§]actually the energy blocked by one particle, because we inverted our raw images

[¶]for small particle densities it is reasonable to minimize the global distance, i.e. the sum of the distances of all particles in subsequent images. For high densities the calculation of an optimized solution takes too long.

	Variant 1 feature	correction	Variant 2 feature	correction	Variant 3 feature	correction
r	\sqrt{A} (1st)	\bar{g} (2nd)	r^* (1st)	$\frac{\text{grad}^2}{r^*}$ (1st)	$\sqrt{A\bar{g}}$ (1st)	\bar{g} (2nd)
z	\bar{g} (1st)	exp in r	grad (1st)	-	$\log(-\text{Laplace}\frac{g_c}{r})$ (2nd)	r and z' (2nd)
q	$g_c > 0.92$		$g_c > 0.18 \wedge \text{Laplace} < 0$		$g_c > 0.92$	

Table 1. Polynomial fits (noted when another fit was used) in given features to order in brackets used for evaluation of r and z . Here, z' stands for an intermediate result of the calculation before the correction was performed. The last row gives a condition, which indicates, if this object should be counted or not. If an object does not meet these requirement the determined r and z will have a large error.

This number is the area density, which must be divided by z_{\max} of the corresponding radius interval to yield the particle radius volume density.

Calibration and validation

To calibrate the setup, depth series of targets with defined radii are recorded. Figure 5 shows some examples of recorded calibration curves. In table 1 the combination of used features for determining r and z are shown. In the last row, a condition is given, which tells us if the data has a certain level of quality. The maximum measurement depth for different radii was determined by searching the depth interval, in which the different algorithms could detect an object for all sequences. To get $z_{\max}(r)$ for all r a linear fit in r was made. The results can be seen in fig. 7 left. In the final evaluation, bubbles with radii smaller than 12 px were detected with variant 3, bubbles with bigger radii were detected either with variant 1 or variant 2.

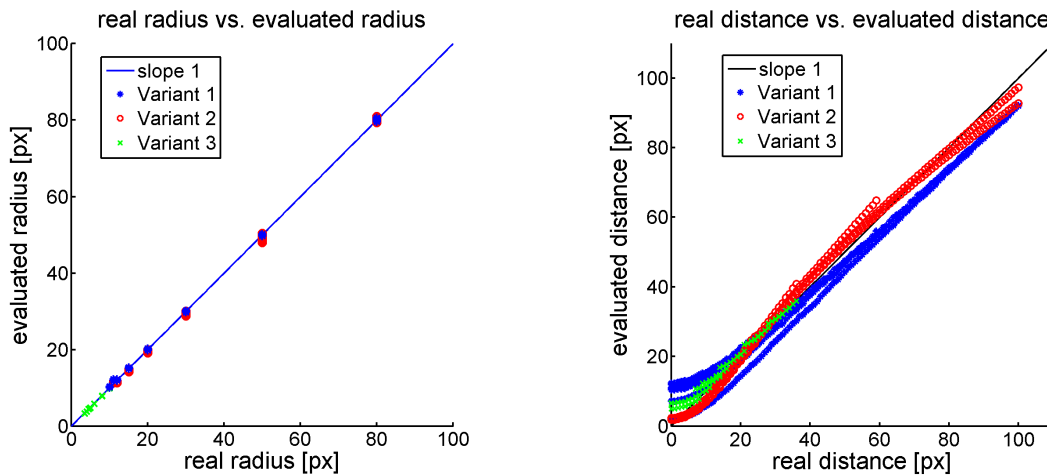


Figure 5. *left:* Calibration curve for the radius. The known radius of the gauge targets are plotted against the radius evaluated with the different algorithms. *right:* Calibration curve for the distance. The known distance of the gauge targets are plotted against the distance evaluated with the different algorithms. For small distances the deviation from the real distance is getting larger.

It is important to note that in bubble measurements the z component has to be multiplied with the refractive index of water when a calibration in air is used. This effect results from the changed angle of the light rays due to refraction (see [8] for more information).

To test the algorithms accuracies several tests were performed. First, the systematic errors were determined by running the algorithms on the gauge data. This error can be further reduced by using more complex functions for the fits, which will increase the computing time. This was not necessary for this application, since the accuracy is good enough. The results of these test are shown in fig. 6. The different approaches are color coded. To test

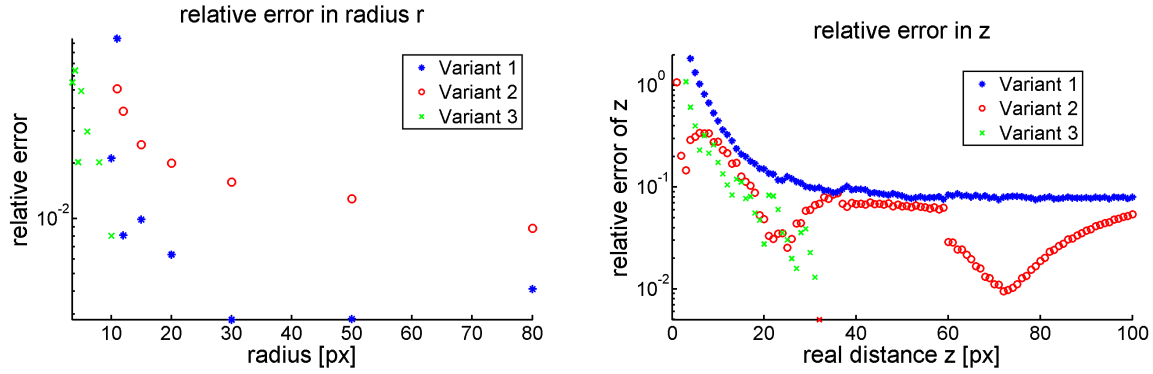


Figure 6. *left:* average relative error of r in dependency of r *right:* average relative error of z in dependency of r .

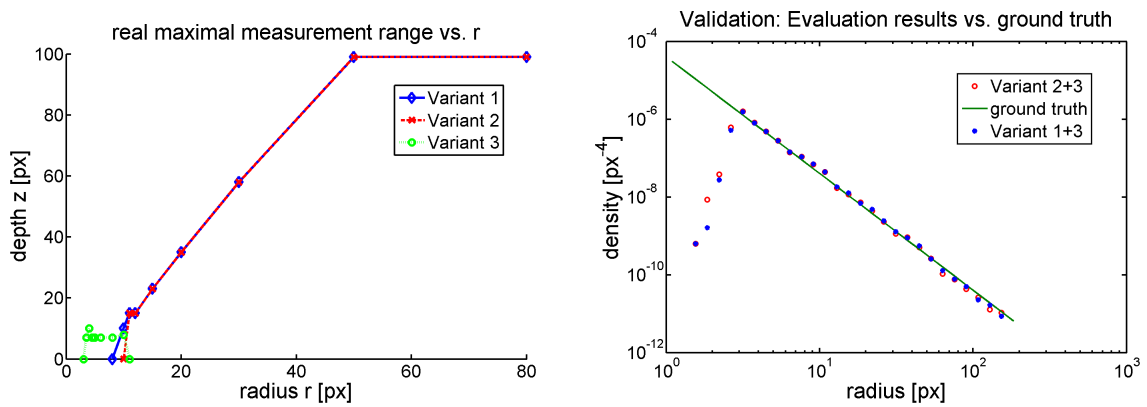


Figure 7. *left:* Maximal measurement depth for all algorithms. The plateau for distances greater than 100 px is due to the calibration data. It was only generated up to 100 depth units. *right:* Comparison of ground truth of sample data set with the results of evaluation with the different algorithms. The deviation for small radii is due to the detecting limit of Variant 3.

the algorithms at high densities, synthetic images were generated and a noise level comparable to the camera noise was added. Since the distribution of the synthetic images is known, it can be compared to the one calculated by the algorithms. The result of this test can be seen in fig. 7 right.

Discussion of the processing method

Fig. 6 shows that it is possible to determine the depth z with an average error of 10%. The error around the focal plane is much larger than far from the plane. Since the distance is not used for the density measurements this large error is not introduced to those measurements. The maximum depth is determined through a linear fit, where the error can be considered below 10%.

The biggest difference of the algorithms is their measurement range. Variant 1 and 2 share almost the same range of 12 px - 300 px, while Variant 3 has a much smaller range but is capable of detecting smaller particles of sizes as small as 3 px (43.5 μm with used optics). The difference of Variant 1 and 2 can be seen at high densities or at distributions with large particles, where Variant 2 can benefit from the cluster separating mechanism.

From the performance point of view Variant 1 is the fastest, followed by Variant 3 and Variant 2 being the slowest, because of the FFT used in the cluster separating. When operating at the resolution limit of this setup and in case of high abundance of smaller bubbles, Variant 3 will take a long time only due to the amount of objects to process. Although variant 3 is not as accurate as the other algorithms, it can use information the other algorithms would ignore.

The accuracy of the velocity measurements is limited by the determination of the center of gravity of the images of the particles. So with appropriate experimental setting it is easily possible to obtain an error below 1%.

Experiments

Two test experiments have been carried out - one for bubbles, one for spray - to demonstrate the method's applicability in realistic laboratory conditions.

Kyoto High wind-speed wind wave channel (bubble size distribution and velocity distribution)

In this experiment the bubble size distribution in presence of breaking waves was measured. Fig. 8 shows the distribution for a wind speed of about 42 m/s at a fetch of 8.8 m. The results are show a power law dependence of the size distribution, which is in accordance to the expectations [1].

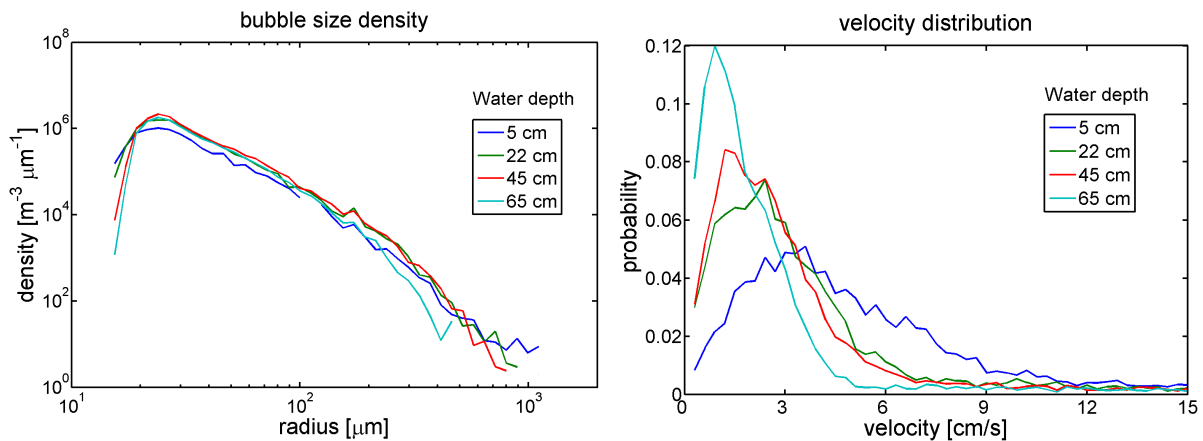


Figure 8. *left:* Size distribution. The cut-off for small radii is due to the detection limit of the algorithms. *right:* velocity distribution at different water depths. This data is recorded at a fetch of 8.8 m at a free stream velocity of 42 m/s in the air phase. Velocity data is integrated over all bubble sizes.

Heidelberg linear wind wave channel/LIZARD (spray size distribution)

Here a supplemental measurement of the size distribution of a spray generated for PIV measurements was conducted. The results agree well with the information given from the manufacturer of the generator, which gives a peak size of 20 μm radius. This size distribution was used to get an idea how much the gravity of the droplets and disturbance of the flow affects the PIV measurements [3].

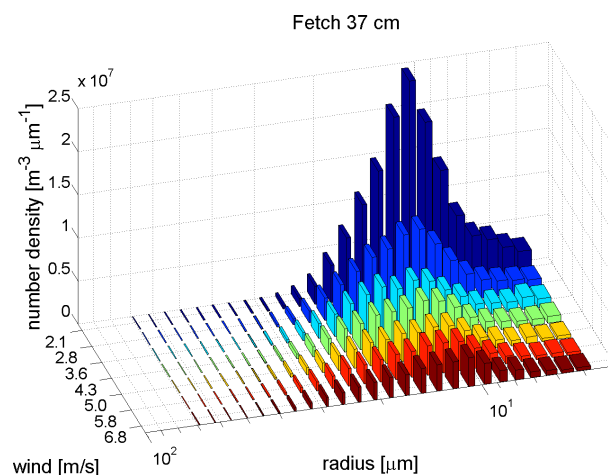


Figure 9. Spray size distribution measurements on a linear wind wave channel in Heidelberg (LIZARD).

Summary and Conclusions

With a remarkably simple experimental setup in conjunction with suitable image processing algorithms, it is possible to measure bubble/spray size and velocity distributions. It is possible to detect bubbles in the radius range of 40-5000 μm with an error below 10% and their measurement volume. With the use of adjusted optics it is also possible to get to even smaller bubble sizes. Optics were tested which can detect bubbles down to radii of 10 μm . Further improvements are still required to extend the measurements to smaller bubble/droplet sizes and higher bubble densities, while preserving the large range of detectable radii.

Acknowledgements

We like to thank Prof. Satoru Komori and his group from Kyoto University for their hospitality and the opportunity to conduct these measurements. We particularly want to thank his assistant professor Naohisa Takagaki, and Koji Iwano for supporting our work. We also gratefully acknowledge funds to initiate the cooperation with Kyoto University and a six week stay of K. Krall & W. Mischler for the measurements in Kyoto through the “Global Networks” program within the “Institutional Strategy to Promote Top-Level Research of Heidelberg University” (ZUK 49/1 Global Networks: Projekt D801000/11.003).

References

- [1] G. De Leeuw and L.H. Cohen. Measurements of oceanic bubble size distributions. 2:II/694–II/699 vol.2, sep 1994.
- [2] Grant B. Deane and M. Dale Stokes. Scale dependence of bubble creation mechanisms in breaking waves. *Nature*, 418(6900):839–844, August 2002.
- [3] Philipp Eger. Messung der Luftströmung über kleinskaligen Wasserwellen mittels Particle Streak Velocimetry in einem linearen Wind-Wellen-Kanal. Bachelor thesis, Institut für Umweltphysik, Fakultät für Physik und Astronomie, Univ. Heidelberg, 2012.
- [4] Markus Honkanen, Pentti Saarenrinne, Tuomas Stoor, and Jouko Niinimäki. Recognition of highly overlapping ellipse-like bubble images. *Measurement Science and Technology*, 16(9):1760–1770, September 2005.
- [5] B. Jähne and P. Geißler. Depth from focus with one image. In *Proc. Conference on Computer Vision and Pattern Recognition (CVPR '94), Seattle, 20.-23. June 1994*, pages 713–717, 1994.
- [6] B. Jähne and P. Geißler. An imaging optical technique for bubble measurements. In M. J. Buckingham and J. R. Potter, editors, *Proc. Sea Surface Sound '94*, pages 290–296, Singapore, 1995. World Scientific.
- [7] Ira S. Leifer, William E. Asher, and Paul J. Farley. A validation study of bubble mediated air-sea gas transfer modeling for trace gases. In B. Jähne and E. Monahan, editors, *Air-Water Gas Transfer, Selected Papers, 3rd Intern. Symp. on Air-Water Gas Transfer*, pages 269–283, Hanau, 1995. AEON.
- [8] Wolfgang Mischler. Entwicklung eines Experiments zur Messung von Blasendichten und blaseninduziertem Gasaustausch. Diplomarbeit, Institut für Umweltphysik, Fakultät für Physik und Astronomie, Univ. Heidelberg, 2010.
- [9] Wolfgang Mischler, Roland Rocholz, and Bernd Jähne. Experimental setup for the investigation of bubble mediated gas exchange. In S. Komori, W. McGillis, and R. Kurose, editors, *Gas Transfer at Water Surfaces 2010*, pages 238–248, 2011.
- [10] G. Rojas and M. R. Loewen. Fiber-optic probe measurements of void fraction and bubble size distributions beneath breaking waves. *Experiments in Fluids*, 43:895–906, 2007.
- [11] S. Vagle and D.M. Farmer. A comparison of four methods for bubble size and void fraction measurements. *Oceanic Engineering, IEEE Journal of*, 23(3):211–222, July 1998.